22

Elastic scattering

Electron scattering studies of nuclear and nucleon structure came into their own with the beautiful experiments at the High Energy Physics Laboratory (HEPL) at Stanford University by Hofstadter and collaborators in the 1950's. These experiments measured charge distributions through elastic scattering [Ho56]. Early results throughout the periodic system from Mg to Pb were summarized in terms of a two-parameter "Fermi model" charge distribution

$$
\begin{aligned}
\rho &= \frac{\rho_0}{1 + e^{(r-R)/a}} \\
R &= r_0 \, A^{1/3} \\
r_0 &\approx 1.07 \, \text{fm} \\
t &\approx 2.4 \, \text{fm}
\end{aligned}
\tag{22.1}
$$

Here the *surface thickness t* is the 90% to 10% fall-off distance ($t \approx 2a \ln 9$). The observed distributions are illustrated in Fig. 22.1. It is difficult to overstate the impact of these experiments. One could actually *see* what the tiny nucleus at the center of the atom looks like.[1] The density of the *nuclear matter* at the center of the nucleus is approximately constant from nucleus to nucleus, as is the surface structure. As one adds nucleons, the nucleus simply grows in size. If fact, it grows exactly as a drop of water grows when more liquid is added to it. The volume of the nucleus is simply proportional to the number of nucleons

$$
V = \frac{4}{3}\pi R^3 = \frac{4}{3}\pi r_0^3 A
\tag{22.2}
$$

---

[1] Experiments on finite-size effects in the spectra of mu-mesic X-rays had previously yielded good values for the nuclear mean-square radius [Fi53].
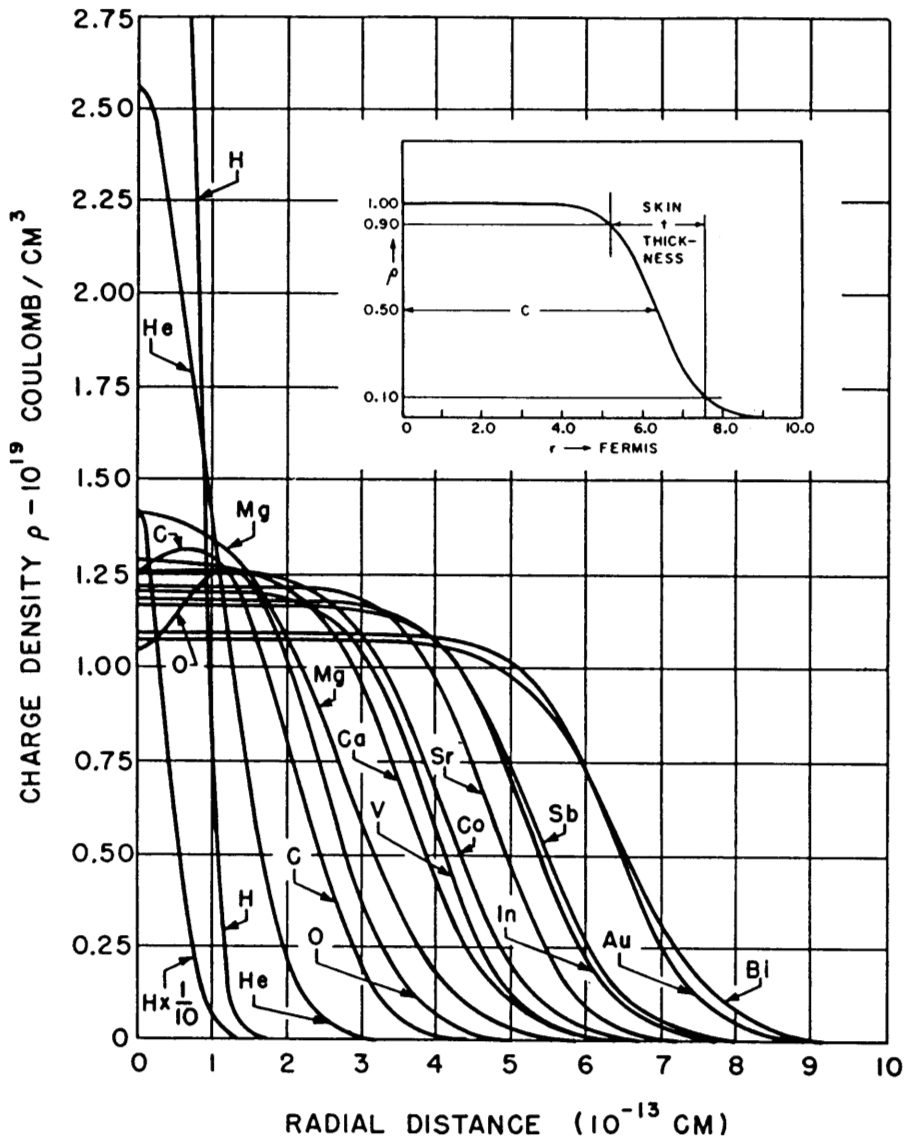
182

Fig. 22.1. Approximate shapes of the charge distribution of selected nuclei, including the proton and alpha particle. Note the change of scale for the proton. The insert explains the Fermi model (here $c \equiv R$) [Ho56].

Furthermore, Hofstadter and collaborators demonstrated that the charge distribution of the proton is of finite extent, with a root-mean-square radius of [Ch56, Ho56]

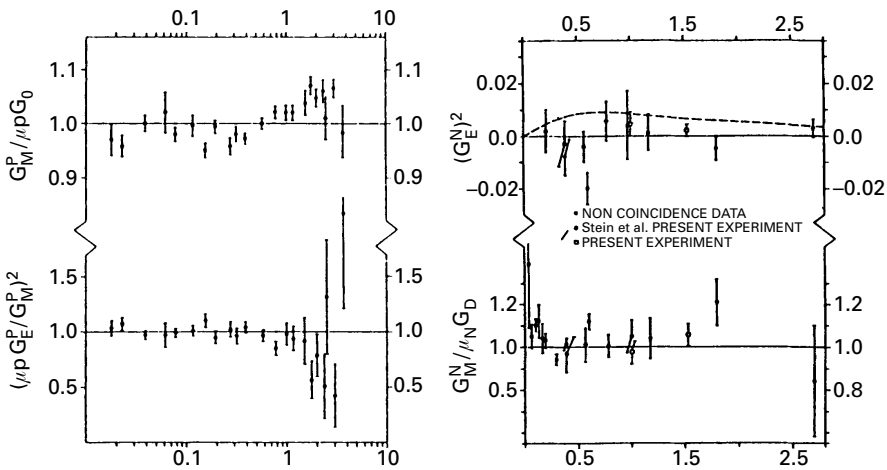$$\langle r_p^2 \rangle^{1/2} \approx 0.77 \, \text{fm} \tag{22.3}$$

Fig. 22.2. Compilation of the form factors of the proton. Left: $(\mu_p G_{\mathrm{E}}^p / G_{\mathrm{M}}^p)^2$ and $G_{\mathrm{M}}^p / \mu_p G_{\mathrm{D}}$ are plotted versus q^2 on a logarithmic scale. Right: $(G_{\mathrm{E}}^n)^2$ [the dashed curve is $G_{\mathrm{E}}^n(q^2) = -\tau G_{\mathrm{M}}^n(q^2)$ with $\tau \equiv q^2/4m^2$] and $G_{\mathrm{M}}^n / \mu_n G_{\mathrm{D}}$ [Ba73].

This gave direct evidence that the nucleon itself is a composite structure.[2] To extract accurate charge distributions in electron scattering from heavier nuclei, one has to deal with the Coulomb distortion of the electron wave functions, as well as other corrections [Ye65, Ra87].

Experiments on elastic magnetic scattering from the proton and neutron demonstrated the spatial extent, and measured the spatial distribution, of the magnetization in this $(J^\pi, T) = (\frac{1}{2}^+, \frac{1}{2})$ system. Free neutron targets do not exist, so one uses the next best thing, a neutron lightly bound to a proton in the deuteron ($^2_1$H). Both quasielastic scattering where the neutron is directly ejected, and elastic scattering, have been employed. The latter depends more sensitively on the ground-state deuteron wave function. Of course, the accompanying proton is not really inert, and nuclear physics comes into play in analyzing these experiments. Nevertheless, over the years reliable charge and magnetic form factors have been obtained for both the proton and neutron, and a summary of the elastic form factors for the nucleon is shown in Fig. 22.2. The *Sachs* form factors are defined in terms of the Dirac form factors according to

$$
\begin{aligned}
G_{\mathrm{M}}(q^2) &\equiv F_1(q^2) + 2m F_2(q^2) \\
G_{\mathrm{E}}(q^2) &\equiv F_1(q^2) - \frac{q^2}{2m} F_2(q^2)
\end{aligned}
\tag{22.4}
$$

The dipole form factor, to which the measured values are compared, is

---

[2] Of course, the fact that the magnetic moments of the neutron and proton already deviate so much from the Dirac values (chapter 19) strongly implies the same thing.
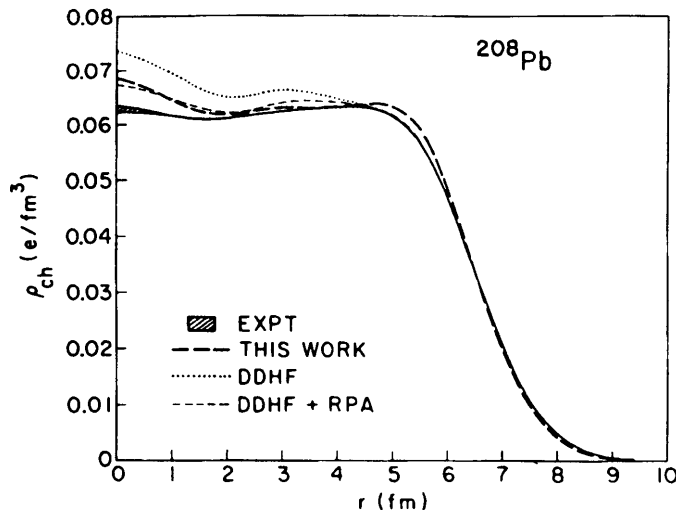
Fig. 22.3. Charge density for $^{208}_{82}$Pb. The solid curve and shaded area represent the fit to the experimental data [He69]. Relativistic mean field theory results are indicated by the long dashed lines [Ho81, Se86]. Some density-dependent Hartree–Fock calculations within the traditional picture are also shown (see [Ho81] for references).

defined by

$$G_{\mathrm{D}} \equiv \frac{1}{(1 + q^2/0.71\,\mathrm{GeV}^2)^2} \tag{22.5}$$

By showing the deviations from the phenomenological dipole form, one can plot the form factors on an expanded scale. Note that at the time of publication of Fig. 22.2, the charge form factor of the neutron was not very well known at all. It is important to emphasize that even though the neutron has no net charge, it can still have a non-uniform spatial distribution of charge within it. One of the advantages of the Sachs form factors is that they have a more direct interpretation in terms of the spatial Fourier transform of the charge and total magnetic moment densities of the nucleon [Wa59]. The theoretical understanding of the charge distribution of nuclei within the traditional picture is based on self-consistent Hartree–Fock calculations of nuclear ground states [Fe71, Go79, Ne82]. The most sophisticated of these use as an interaction the local-density T-matrix calculated in the Brueckner theory of nuclear matter [Ne82]. Relativistic mean field theory (RMFT), described in the previous section, gives a very direct determination of these densities with a local interaction. In Fig. 22.3 we show the comparison of the RMFT calculation by Horowitz and Serot
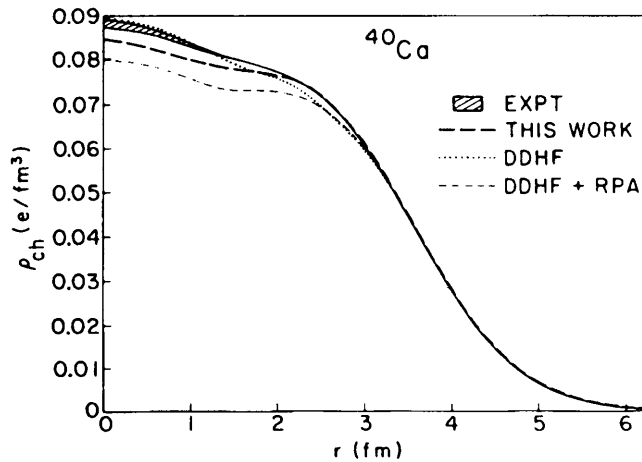
Fig. 22.4.   As Fig. 22.3, but for $^{40}_{20}$Ca [Fr79, Ho81, Se86].

of the charge density of $^{208}_{82}$Pb and the experimental determination of this quantity [Ho81, Wa95]. The error band on the experimental charge distribution arises primarily from the fact that one is always measuring only a partial Fourier transform in electron scattering, although other effects contribute [Fr73]. It is from this figure that the density of nuclear matter is determined [Ho81]. Figure 22.4 shows a similar result for $^{40}_{20}$Ca [Ho81, Wa95]. Here the half-density radius determines the scalar mass [Ho81]. All other nuclear charge densities are then predicted in RMFT (see Fig. 21.5). In summary, although in a sense it is the simplest thing one can compute [Se97], one has a good theoretical understanding of the ground-state charge densities of nuclei.

The theoretical analysis of the elastic form factors of the nucleon proceeds most directly through the *spectral representation* of these quantities [Ch58, Fe58, Dr61, Wa95]. From very general field theory principles, one establishes that the isovector and isoscalar form factors of the nucleon have the representations

$$
\begin{aligned}
F_i^V(q^2) &= \frac{1}{\pi}\int_{(2m_\pi)^2}^{\infty}\frac{w_i^V(\sigma^2)\,d\sigma^2}{\sigma^2+q^2} \qquad ; \; i=1,2 \\
F_i^S(q^2) &= \frac{1}{\pi}\int_{(3m_\pi)^2}^{\infty}\frac{w_i^S(\sigma^2)\,d\sigma^2}{\sigma^2+q^2}
\end{aligned}
\tag{22.6}
$$

Here m_π is the pion mass. The thresholds in the representations in Eqs. (22.6) are obtained by angular momentum, isospin, and charge-conjugation considerations.

The real spectral weight functions $w_i^{S,V}(\sigma^2)$ are related to the absorptive

part of the amplitude for a time-like virtual photon to go through an intermediate hadronic state and then into a nucleon–antinucleon pair. Time-like virtual photons with $q = (\mathbf{0}, iW)$ can be created in the laboratory through the process of electron–positron annihilation in the C-M system. The process $e^+ + e^- \rightarrow pions$ can be measured experimentally for any $W \geq 2m_\pi$. The amplitude for $e^+ + e^- \rightarrow N + \bar{N}$ can be accessed experimentally only for $W \geq 2m$; for $W < 2m$, one needs analytic continuation.

The spectral representations in Eqs. (22.6) hold in the entire q^2 plane. The representation for the charge form factors probably requires one subtraction [Dr61]

$$ F_1^\alpha(q^2) = 1 - \frac{q^2}{\pi} \int \frac{w_1^\alpha(\sigma^2)\, d\sigma^2}{\sigma^2(\sigma^2 + q^2)} \qquad ; \alpha = S, V \qquad (22.7) $$

One can readily establish that in elastic electron scattering from the nucleon there is always one Lorentz frame, the so-called Breit (or brick-wall) frame, where the electron undergoes no energy transfer. In this frame, the four-momentum transfer takes the form $q = (\mathbf{q}, i0)$. In this case one can define the form factor as the three-dimensional Fourier transform of a charge and magnetization density according to[3]

$$
\begin{aligned}
F(\mathbf{q}^2) &= \int d^3x\, e^{i\mathbf{q}\cdot\mathbf{x}}\, \rho(r) \\
\rho(r) &= \int \frac{d^3q}{(2\pi)^3}\, e^{-i\mathbf{q}\cdot\mathbf{x}}\, F(\mathbf{q}^2)
\end{aligned}
\qquad (22.8)
$$

Insertion of Eqs. (22.6) in the second relation gives

$$ \rho(r) = \frac{1}{4\pi^2} \int d\sigma^2\, w(\sigma^2)\, \frac{e^{-\sigma r}}{r} \qquad (22.9) $$

This relation expresses the density as a linear combination of Yukawa distributions, each of mass σ. By the uncertainty principle, the mass σ of the intermediate state determines how far it extends out from the origin. The intermediate state now occurs as a virtual one in electron scattering where the momentum transfer is space-like.

Consider a simple example of these ideas. The lightest mass hadron is the pion, and it is evident from Eq. (22.9) that charged pions are responsible for the long-range part of the electromagnetic structure of the nucleon. To evaluate the two-pion contribution to the spectral weight function for $F_2(q^2)$ in Born approximation (without pion rescattering) one can simply look at the Feynman diagram for the lowest-order vertex correction illustrated in Fig. 22.5. We calculate the contribution of this diagram to S_{fi}

---

[3] The Wigner–Eckart theorem and parity invariance imply that the ground state densities must be spherically symmetric for a spin one-half system.
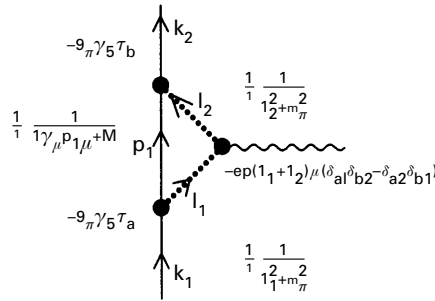
Fig. 22.5.   Two-pion contribution to S_{fi} and $F_2(q^2)$ in Born approximation.

from the following pion–nucleon and pion–photon lagrangian densities[4]

$$\mathcal{L}_{\pi N} = ig_\pi \bar{\psi} \gamma_5 \boldsymbol{\tau} \ \psi \cdot \boldsymbol{\pi}$$

$$\mathcal{L}_{\gamma\pi} = -e_p \left[\boldsymbol{\pi} \times \frac{\partial \boldsymbol{\pi}}{\partial x_\mu} \right]_3 A_\mu \qquad (22.10)$$

The component contributions to the diagram are then indicated in Fig. 22.5. It is a nice exercise to show that the result from this diagram can be put into the following form

$$2mF_2(q^2) = \tau_3 \frac{g_\pi^2}{4\pi} \int_0^1 dx \, (1-x)^2 \int_0^x dy \, \frac{m^2}{m^2(1-x)^2 + m_\pi^2 x + q^2 y(x-y)} \qquad (22.11)$$

The spectral representation and two-pion contribution to the spectral weight function follow directly. Note that this contribution is entirely isovector.

The integral in Eq. (22.11) is well-defined, and one can use it to calculate this two-pion contribution to the anomalous magnetic moment of the nucleon by simply evaluating $2mF_2(0)$. The longest range two-pion contribution to the mean-square radius of the isovector magnetic moment can be obtained through

$$\frac{F_2^V(q^2)}{F_2^V(0)} = 1 - \frac{q^2}{6} \langle r^2 \rangle_2^V + \cdots \qquad (22.12)$$

The use of $g_\pi^2/4\pi = 14.4$ from pion–nucleon scattering leads to the results shown in Table 22.1. The present analysis provides a qualitative, and even semiquantitative, understanding of the anomalous magnetic moment and its mean-square radius [Ch58, Fe58].

To pursue this approach even further, it was argued *before their discovery* that vector mesons with $(J^\pi, T) = (1^-, 1)$ and $(1^-, 0)$, the ρ and ω, must be

---

[4] The absorptive part is independent of the particular form of the π–N coupling used.

Table 22.1. Two-pion contribution to the anomalous magnetic moment of the nucleon in Born approximation.

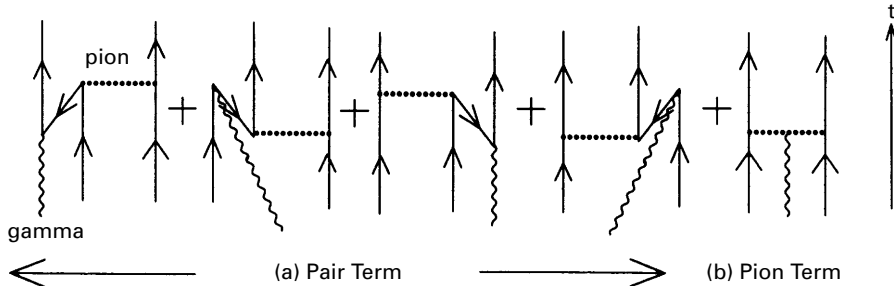|	λ'^S	λ'^V	$\langle r^2 \rangle^V_{mag}$	$(\langle r^2 \rangle^V_{mag})^{1/2}$
Theory	0	3.20	0.24 fm^2	0.49 fm
Experiment	-0.12	3.706	≈ 0.64 fm^2	≈ 0.80 fm

Fig. 22.6. Time-ordered Feynman diagrams retained in the one-pion exchange current calculation in [Du76].

present to make the *size* of the distributions quantitative [Na57, Fr60]. The basic idea is that a two- or three-pion resonance makes the distribution extend out further.[5]

Of course, the internal quark structure of the nucleon plays an essential role in determining the electromagnetic structure of the nucleon (chapter 24); however, it is clear from Eq. (22.9) that pions are responsible for the long-range contribution to this structure. Both elements of the internal structure clearly play a role.[6] Effective chiral lagrangians that reflect the underlying symmetry structure of QCD, and chiral perturbation theory, place the calculation of the the long-range low-q^2 pion contribution to the nucleon form factors on a firmer theoretical foundation [Be98, Ku01].

A prime example of the need for an explicit hadronic description of nuclei is provided by the additional two-body currents arising from the exchange of charged mesons between nucleons. Although many exchange current calculations exist, for concreteness we briefly describe those of Dubach, Koch, and Donnelly [Du76]. These authors keep the static limit [leading $O(1/m)$] of the time-ordered Feynman diagrams shown in Fig. 22.6. Each of these processes clearly represents an additional contribution

---

[5] In chapter 21 we were content to include the contribution of charged mesons to the internal structure of the nucleon in a phenomenological fashion, through a single-nucleon form factor $f_{SN}(q^2) = G_D(q^2)$.

[6] "Bag models" and "chiral soliton models" attempt to incorporate both elements of this internal structure [Wa95].

to the current in the traditional picture, which is now extended to

$$\hat{J}_\mu(\mathbf{x}) = \sum_{i=1}^{A} J_\mu^{(1)}(\mathbf{x}_i; \mathbf{x}) + \sum_{i<j=1}^{A} J_\mu^{(2)}(\mathbf{x}_i, \mathbf{x}_j; \mathbf{x}) \qquad (22.13)$$

The two-body current can be identified through reproduction of the S-matrix as follows.

The free Dirac propagator can be decomposed according to [Fe71, Wa95]

$$\frac{1}{i\gamma_\mu p_\mu + m} \equiv \left[\frac{1}{2E_p} \frac{\boldsymbol{\alpha} \cdot \mathbf{p} + \beta m + E_p}{E_p - p_0 - i\eta} + \frac{1}{2E_p} \frac{\boldsymbol{\alpha} \cdot \mathbf{p} + \beta m - E_p}{E_p + p_0 - i\eta} \right] \beta \qquad (22.14)$$

The first term yields the usual non-relativistic result [Fe71]; the second term gives rise to backward propagation in time. The Feynman rules from the lagrangian in Eq. (22.10) allow one to evaluate the contribution to the S-matrix from the graphs in Fig. 22.6, retaining just the second piece of the baryon propagator. An equivalent S-matrix can be constructed from the current in Eq. (22.13), and one can then identify the additional two-body current. Define

$$J_\mu(\mathbf{x}_1, \mathbf{x}_2; \mathbf{x}) = \int e^{i\mathbf{k}\cdot\mathbf{x}} J_\mu(\mathbf{x}_1, \mathbf{x}_2; \mathbf{k}) \frac{d^3k}{(2\pi)^3} \qquad (22.15)$$

Then to leading order in $1/m$, and with the neglect of k_0, the pair contribution to the pion-exchange current in Fig. 22.6(a) is given by

$$\mathbf{J}^{\text{pair}}(\mathbf{x}_1, \mathbf{x}_2; \mathbf{k}) = -e_p f_\pi^2 [\boldsymbol{\tau}^{(1)} \times \boldsymbol{\tau}^{(2)}]_3$$
$$\times \left\{ \boldsymbol{\sigma}_2 \left(\frac{\boldsymbol{\sigma}_1 \cdot \mathbf{r}}{r} \right) e^{-i\mathbf{k}\cdot\mathbf{x}_2} + \boldsymbol{\sigma}_1 \left(\frac{\boldsymbol{\sigma}_2 \cdot \mathbf{r}}{r} \right) e^{-i\mathbf{k}\cdot\mathbf{x}_1} \right\} \left(\frac{1 + x_\pi}{x_\pi^2} \right) e^{-x_\pi} \qquad (22.16)$$

Here

$$\mathbf{x}_\pi = \mu\mathbf{r} \qquad\qquad ; \mu \equiv m_\pi$$
$$\mathbf{r} = \mathbf{x}_1 - \mathbf{x}_2 \qquad\qquad ; \mathbf{R} = \frac{1}{2}(\mathbf{x}_1 + \mathbf{x}_2)$$
$$f_\pi^2 = \frac{g_\pi^2}{4\pi} \left(\frac{\mu}{2m} \right)^2 = 0.080 \qquad (22.17)$$

The pion contribution in Fig. 22.6(b) is

$$\mathbf{J}^{\text{pion}}(\mathbf{x}_1, \mathbf{x}_2; \mathbf{k}) = e_p \left(\frac{f_\pi}{\mu} \right)^2 [\boldsymbol{\tau}^{(1)} \times \boldsymbol{\tau}^{(2)}]_3 (\boldsymbol{\sigma}_1 \cdot \boldsymbol{\nabla}_1)(\boldsymbol{\sigma}_2 \cdot \boldsymbol{\nabla}_2)$$
$$\times \int_{-1/2}^{1/2} dv (-irv\mathbf{k} + \mathbf{y}) \left(\frac{e^{-y}}{y} \right) \exp\{-i\mathbf{k} \cdot (\mathbf{R} - v\mathbf{r})\} \qquad (22.18)$$

Here

$$\mathbf{y} = \mathbf{r}\left[\mu^2 + \left(\frac{\mathbf{k}^2}{4}\right)(1-4v^2)\right]^{1/2} \tag{22.19}$$

There is no exchange contribution to the charge density to this order in $1/m$. These results are from [Du76], and the reader is now in a position to reproduce them.[7]

This exchange current has the following features to recommend it:

- If the current is taken to be the sum of the one-body current of chapter 19 and the above exchange current, and if a two-nucleon potential has the form $V = V^{\text{neutral}} + V^{\text{OPEP}}$ where the last term is the one-pion exchange potential [Wa95], then the current is differentially conserved [Du76]

$$\frac{\partial \hat{J}_\mu}{\partial x_\mu} = \nabla \cdot \hat{\mathbf{J}} + i[\hat{H}, \hat{\rho}] = 0 \tag{22.20}$$

- The threshold pion electroproduction part of the graphs in the above amplitude satisfies the Kroll–Ruderman (soft-pion) theorem;

- This one-pion contribution represents the longest-range part of the two-body exchange current; it is exact as $|\mathbf{x}_1 - \mathbf{x}_2| \to \infty$;

- The charge density operator is unmodified to leading $O(1/m)$; hence transition matrix elements of the charge density can be used to calibrate the nuclear structure in exchange-current calculations.

Assume that $^3_2$He can be described by a $(v1s_{1/2})^{-1}$ harmonic oscillator shell model configuration as shown in Figs. 20.7 and 20.8. The magnetic moment calculated with the inclusion of the above exchange current is $\mu = -2.078$ n.m., now closer to the experimental value $\mu = -2.127$ n.m. than is the Schmidt value $\mu = -1.913$ n.m. in Table 20.1. (Here 1 n.m. $= e_p\hbar/2m_pc$). This gives one some confidence in the present exchange current calculation [Du76]. The effect on elastic magnetic electron scattering at modest momentum transfers, say $q^2 \leq 6 \text{ fm}^{-2}$, is shown in Fig. 22.7; the effect is not large. This illustrates the *marginal* role of exchange currents in the traditional nuclear physics domain.[8]

Figure 22.8 illustrates the state of the art with elastic magnetic scattering from $^3_2$He [Ca82]. The measurements are from Saclay and Bates. The dashed line shows the result obtained from the best three-body calculation

---

[7] Use $(ab)^{-1} = \int_0^1 dz [az + b(1-z)]^{-2}$.
[8] A relativistic QHD calculation of this exchange current, without the $1/m$ expansion, is contained in [Bl91].
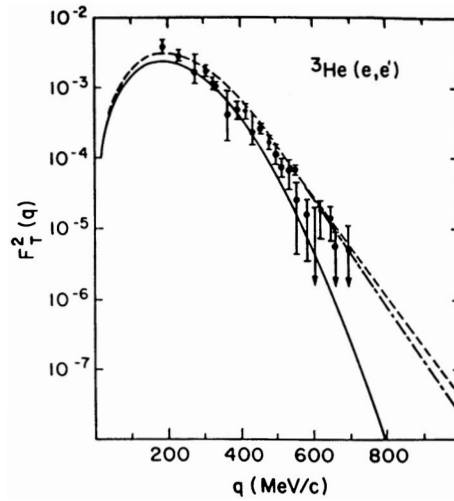
Fig. 22.7. Elastic transverse form factor for $_{2}^{3}$He(e, e') in the harmonic oscillator model with (dashed) and without (solid) one-pion exchange currents [Du76, Wa84].
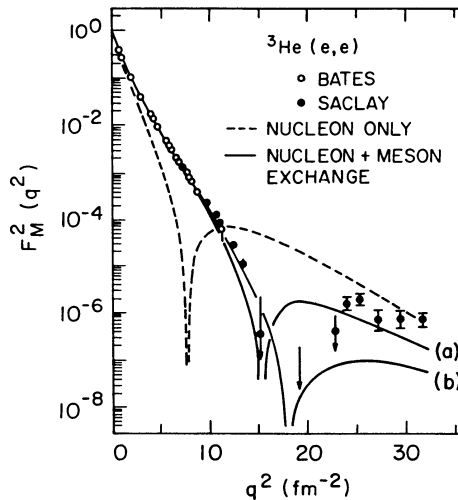

Fig. 22.8. Elastic magnetic form factor for $_{2}^{3}$He(e, e) out to high q^2 [Ca82]. Two exchange-current theories are shown: (a) from [Ha83]; (b) from [Ri80].

done in the traditional picture; the three-body wave function is obtained by solving the Faddeev equations with potentials fitted to two-body data, and the current is obtained from the properties of free nucleons. There is clear disagreement with the data as q^2 increases to $\sim 10\,\mathrm{fm}^{-2}$, not by a few percent, but by orders of magnitude. The best three-body calculation in
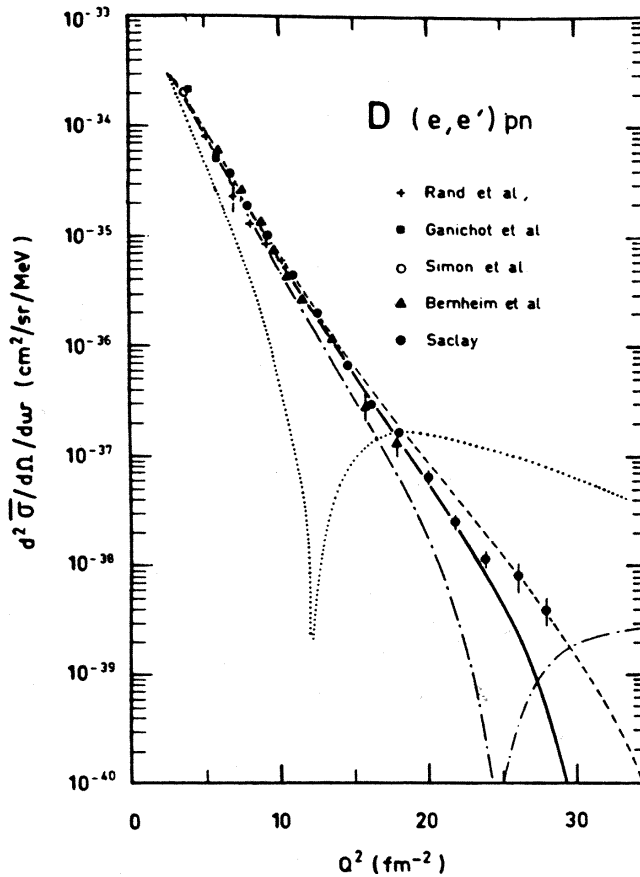
Fig. 22.9. Cross section for $^2_1\mathrm{H}(e, e')pn_{thresh}$. The dotted curve is the impulse-approximation result, the dash-dot curve includes the pion-exchange contribution, the dash curve includes also a ρ-exchange contribution, and the solid curve is the total result, which includes a Δ contribution. [Au85].

the traditional picture clearly fails at high q^2. Also shown in Fig. 22.8 are two exchange-current calculations that include the pion exchange current discussed above, as well as other hadronic contributions [Ha83, Ri80]. The difference between these two curves at high q^2 is a good measure of the present theoretical uncertainty. While the exchange current contribution is marginal at low momentum transfers, it is a *dominant* effect at large q^2. A more recent and extensive discussion of electromagnetic interactions with light nuclei is contained in [Ca91].

This pion exchange current also shows up dramatically in threshold electrodisintegration of the deuteron $^2_1\mathrm{H}(e, e')pn_{thresh}$ as shown in Fig. 22.9 [Au85].